EFFECTS OF HEAT RELEASE ON THE TURBULENCE STRUCTURE IN TEMPORALLY EVOLVING COMPRESSIBLE MIXING LAYERS

Inga Mahle, Rainer Friedrich
Fachgebiet Strömungsmechanik, Technische Universität München
Boltzmannstr. 15, D-85748 Garching, Germany
inga.mahle@aer.mw.tum.de

Holger Foysi, Sutanu Sarkar
UC San Diego,
9500 Gilman Drive, La Jolla, CA 92093, USA

ABSTRACT

The aim of this work is to investigate and explain effects of compressibility and heat release on turbulence, in particular on the dynamics of pressure fluctuations and the pressure-strain correlations. To this end, we perform and analyze highly resolved DNS of temporally evolving inert and reacting compressible mixing layers at three different convective Mach numbers. The particular focus of the analysis is on the question whether mean density effects play the key role also in the reacting mixing layer.

INTRODUCTION

Effects of reduced turbulence activity and growth rate of a compressible mixing layer when the convective Mach number increases, are well-known phenomena. That heat release due to combustion has similar effects, seems to be less well-known, although it has important implications for applications such as scramjet engines the efficiency of which depends on a proper mixing of oxidizer and fuel.

The growth rate reduction of the inert mixing layer by compressibility was investigated e.g. by Vreman et al. (1996). They found out that the decrease in pressure fluctuations which led to reduced pressure-strain terms is responsible for the changes in growth rate of a plane compressible mixing layer. Pantano and Sarkar (2002) studied inert compressible mixing layers as well and showed by an analysis based on the wave equation for the pressure fluctuations that the reason for the reduction of the pressure-strain correlations is a finite time delay in the transmission of pressure signals from one point to an adjacent point and that the resultant increase in decorrelation leads to a reduction in the pressure-strain correlation. In a reacting shear layer, heat release due to chemical reactions leads to a significant decrease of the mean density. Therefore, it is of interest to see, which role mean density effects play in this case. Such effects were absent in inert compressible homogeneous shear flow (Sarkar, 1995), but were found to be of key importance for the understanding of the reduction of pressure-strain correlations in inert compressible channel flow (Foysi et al. 2004).

The relevance of mean density effects in shear layers is one focus of the present paper, which is organized as follows: The next section gives an overview over the generic configuration, the six test cases with the different convective Mach numbers and the most important features of the numerical simulations. Then, in the main part of the paper, results including instantaneous flow fields and averaged quantities are shown and analyzed. Particular attention is given to the pressure-strain correlations which are investigated with the help of a Green function. In the last section, a summary is given and conclusions are drawn.

Table 1: Computational parameters: L_1, L_2, L_3 are the streamwise, spanwise and transverse domain sizes resolved by N_1, N_2 and N_3 grid points, respectively. $\delta_{\omega,0}$ is the initial vorticity thickness of the shear layer at $Re_{\omega,0} = 640$.

Case	$L_1/\delta_{\omega,0}$ x $L_2/\delta_{\omega,0}$ x $L_3/\delta_{\omega,0}$	N_1 x N_2 x N_3
inert	192.375 x 32.25 x 96.75	768 x 192 x 576
rct.	345 x 86 x 172	768 x 192 x 432

DNS OF INERT AND REACTING COMPRESSIBLE MIXING LAYERS

DNS of inert and reacting temporally evolving mixing layers are performed at three different convective Mach numbers (M_c = 0.15, 0.7 and 1.1). All test cases are 3D with x_1 and x_2 denoting the periodic streamwise and spanwise directions and x_3 the direction of the main shear. Table 1 gives the computational parameters.

In the reacting cases, one stream of the mixing layer contains oxygen and nitrogen and the other hydrogen and nitrogen premixed in a way that the free-stream densities are the same and the stoichiometric mixture fraction is $Z_s = 0.3$. In the inert cases, pure nitrogen mixes with pure oxygen both of which have a similar molecular weight which results in a nearly constant mean density. The schematic configuration is shown in Fig. 1.

Hydrogen chemistry is simplified in order to keep the number of additional variables small: The assumption of one global reaction with infinitely fast reaction rates and a constant common Schmidt number for all species allows

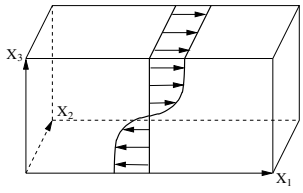

Figure 1: The configuration of temporally evolving shear layers

to relate their mass fractions to a single passive scalar, the mixture fraction Z. In addition to the transport equation of Z, the continuity and the momentum equations, the energy equation is solved to retain a fully compressible formulation, in which dynamic viscosity and heat conductivity depend on local temperature and species mass fractions. The transport equations are integrated in time using a 3rd order low-storage Runge-Kutta scheme and 6th order compact central schemes in space.

The mixing layers were initialized with hyperbolic tangent profiles for the mean streamwise velocity with superimposed random, broadband fluctuations for all velocity components. They rapidly became turbulent and achieved a self-similar state with Reynolds numbers based on instantaneous vorticity thickness and velocity difference between the free streams ranging from 15000 to 35000.

In the following, the inert/ reacting cases are denoted by inert-XX, respectively inf-XX, where XX replaces the convective Mach number.

ANALYSIS AND RESULTS

Instantaneous scalar fields

In order to show that compressibility and heat release attenuate all turbulent fluctuations, we display instantaneous scalar fields as an example at the beginning of the self-similar state. Figures 2 to 3 demonstrate the stabilization of O_2 mass fraction fluctuations in the middle of the computational domain when the Mach number increases. This can be seen clearly when comparing the isolines at 0.1 and 0.9 shown in these figures. For the inert case at low M_c (Fig. 2), they are much more wrinkled than for case inert-1.1 (Fig. 3).

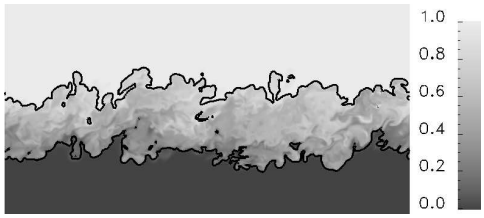

Figure 2: Case inert-0.15: Instantaneous mass fraction of O_2, x_1-x_3-plane, isolines $Y_{O2} = 0.1$ and 0.9 as black lines

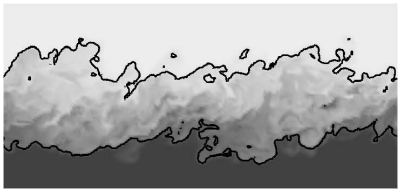

Figure 3: Case inert-1.1: Instantaneous mass fraction of O_2, x_1-x_3-plane, isolines $Y_{O2} = 0.1$ and 0.9 as black lines, same scale as in Fig. 2

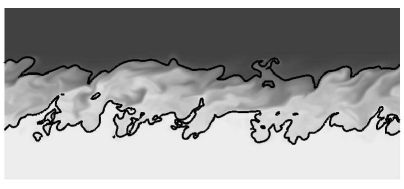

Figure 4: Case inf-1.1: Instantaneous mixture fraction, x_1-x_3-plane, isolines $Z = 0.1$ and 0.9 as black lines, same scale as in Fig. 2

A further smoothening can be observed when heat release sets in (case inf-1.1 in Fig. 4). This is particularly visible from the isoline $Z = 0.1$, which is closer to the flame sheet at $Z_s = 0.3$ than the isoline $Z = 0.9$.

Momentum thickness growth rates

The stabilizing effect of heat release and compressibility is also visible from the temporal development of the momentum thickness,

$$\delta_\theta = \frac{1}{\rho_0 \Delta u^2} \int_{-\infty}^{\infty} \overline{\rho} \left(\frac{1}{4} \Delta u^2 - \widetilde{u}_1^2 \right) dx_3, \qquad (1)$$

which is shown in Figs. 5 and 6 for the inert and reacting test cases, respectively. $\Delta u = u_1 - u_2$ is the velocity difference between the free streams (upper stream: index 1, lower stream: index 2), $\rho_0 = (\rho_1 + \rho_2)/2$ is the reference density and $\overline{\rho}$ the mean density. Here and in the following, $\overline{\bullet}$ denotes a Reynolds averaged quantity and $\widetilde{\bullet}$ a Favre averaged quantity. Primes and double primes indicate the respective fluctuations. From Figs. 5 and 6, it can be seen that the momentum thickness growth rate reduces with increasing compressibility and with heat release. When a self-similar state is reached, constant momentum thickness growth rates are established as shown by the linear regressions.

Mean profiles

During the self-similar state, profiles of flow variables, averaged at different times over the homogeneous directions, collapse when non-dimensionalized appropriately. Therefore, also temporal averages can be taken which is done for all profiles in this and the following sections. Figure 7 shows the Favre averaged streamwise velocity which is not too much influenced by compressibility and heat release. In contrast to this, the mean density is visibly affected by both mechanisms, as seen in Fig. 8. Heat release, in particular

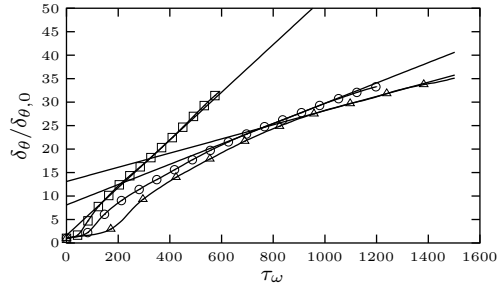

Figure 5: Momentum thickness, normalized by its initial value $\delta_{\theta,0}$, □: inert-0.15, ○: inert-0.7, △: inert-1.1, straight lines show linear regressions for the self-similar state

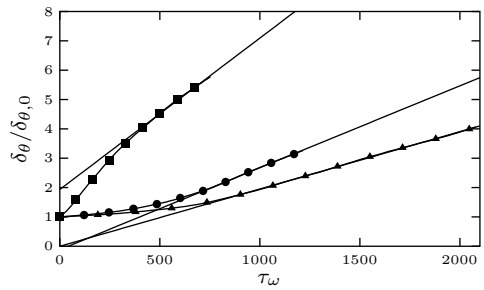

Figure 6: Momentum thickness, normalized by its initial value $\delta_{\theta,0}$, ■: inf-0.15, ●: inf-0.7, ▲: inf-1.1, straight lines show linear regressions for the self-similar state

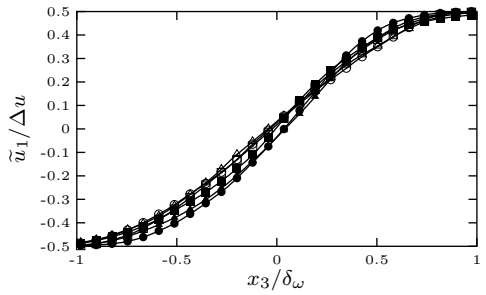

Figure 7: Favre averaged streamwise velocity, normalized by Δu, □: inert-0.15, ○: inert-0.7, △: inert-1.1, ■: inf-0.15, ●: inf-0.7, ▲: inf-1.1

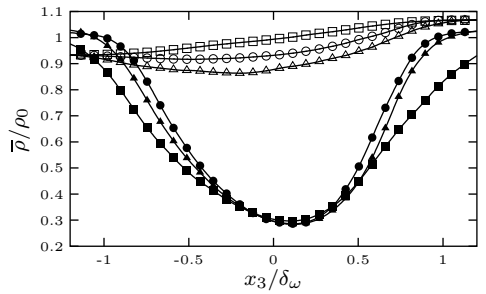

Figure 8: Mean density, normalized by ρ_0, symbols as in Fig. 7

reduces $\overline{\rho}$ strongly due to the high temperatures in the vicinity of the flame sheet. For the inert cases, a decrease of the mean density with increasing M_c is a result of dissipative heating. When reaction sets in, this mechanism is masked in the center by the stronger effect of heat release.

Reynolds stresses and turbulent kinetic energy

When neglecting mean viscous effects, the non-dimensional momentum thickness growth rate is given by (Vreman et al, 1996)

$$\dot{\delta}_\theta = \frac{1}{\Delta u}\frac{d\delta_\theta}{dt} \approx -\frac{2}{\rho_0 \Delta u^3}\int_{-\infty}^{\infty} \overline{\rho u_1'' u_3''}\frac{\partial \widetilde{u}_1}{\partial x_3} dx_3. \qquad (2)$$

From this equation, it can be seen that there are two factors that might be responsible for the reduction of the growth rate by compressibility and heat release: The slope of the Favre averaged streamwise velocity, $\frac{\partial \widetilde{u}_1}{\partial x_3}$, and the Reynolds shear stress $\overline{\rho}R_{13} = \overline{\rho u_1'' u_3''}$. The first quantity has been shown in Fig. 7 to be similar for all mixing layers under investigation. Therefore, a decrease in Reynolds shear stress must be the main cause for the decrease in growth rate. This

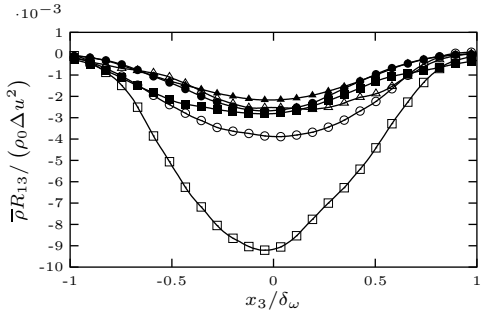

Figure 9: Reynolds shear stress $\overline{\rho}R_{13}$, normalized by $\rho_0\Delta u^2$, symbols as in Fig. 7

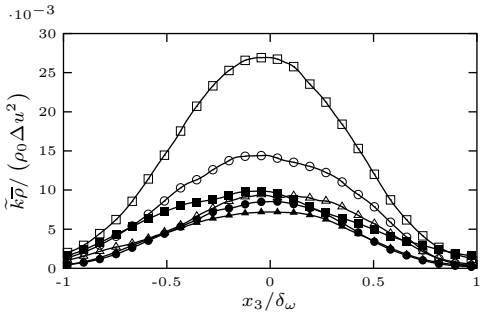

Figure 10: Turbulent kinetic energy, normalized by $\rho_0\Delta u^2$, symbols as in Fig. 7

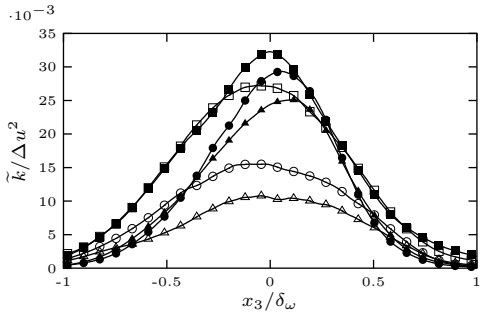

Figure 11: Turbulent kinetic energy, normalized by $\overline{\rho}\Delta u^2$, symbols as in Fig. 7

is confirmed by Fig. 9.

The stabilizing effect of heat release and compressibility on turbulent fluctuations can also be seen from the other Reynolds stresses and is in agreement with what has been concluded from the instantaneous scalar fields (cf. Figs. 2 to 4). Consequently, also the turbulent kinetic energy, $\overline{\rho}\widetilde{k} = \overline{\rho u_i'' u_i''}$, which is shown in Fig. 10, decreases when normalized the same way as the Reynolds shear stress. However, when normalizing in another way, namely with the mean density $\overline{\rho}$ instead of the constant reference density ρ_0, the consequences of heat release are different: heat release causes an increase of $\widetilde{k}$ close to the center of the shear layer (Fig. 11). To understand these differences, consider the low Mach number inert and reacting cases (square open and closed symbols). The reduction of $\overline{\rho}\widetilde{k}$ by heat release in Fig. 10 is a mean density effect, since the two curves collapse in Fig. 11 over most of the domain, except around the center of the shear layer. The increase of $\widetilde{k}$ due to heat release, there, is a consequence of the increase in correlation between Favre velocity fluctuations. The corresponding correlation coefficient (not shown) reflects this behaviour and is in contrast to the behaviour of the correlation between $\rho u_i''$ and u_i''. This also holds for the higher Mach number cases. The effect of compressibility on the other hand has only a weak mean density component for the Mach numbers considered, as concluded from Fig. 8. Its stabilizing effect will later be related to the pressure fluctuations and their determining Poisson equation.

Reynolds stress transport equations

The transport equations of the Reynolds stresses are

$$\frac{\partial \overline{\rho} R_{ij}}{\partial t} + \frac{\partial\left(\overline{\rho}\widetilde{u}_k R_{ij}\right)}{\partial x_k} = P_{ij} - \epsilon_{ij} + T_{ij} + \Pi_{ij} + \Sigma_{ij} \qquad (3)$$

with the production rates P_{ij}, the dissipation rates ϵ_{ij}, the turbulent transport terms T_{ij}, the pressure-strain correlations Π_{ij} and the mass flux coupling terms Σ_{ij}. The

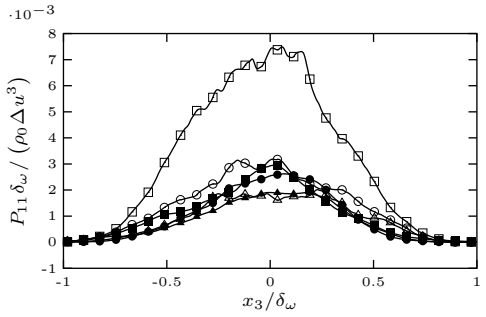

Figure 12: Production rate of streamwise Reynolds stress, normalized by $\rho_0 \Delta u^3/\delta_\omega$, symbols as in Fig. 7

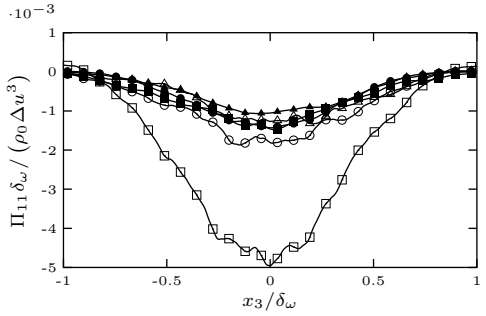

Figure 13: Pressure-strain rate of streamwise Reynolds stress, normalized by $\rho_0 \Delta u^3/\delta_\omega$, symbols as in Fig. 7

influence of compressibility and heat release on the production tensor,

$$P_{ij} = -\left(R_{ik} \frac{\partial \widetilde{u}_j}{\partial x_k} + R_{jk} \frac{\partial \widetilde{u}_i}{\partial x_k} \right), \tag{4}$$

and the pressure-strain rate tensor,

$$\Pi_{ij} = \overline{p' \left(\frac{\partial u_i''}{\partial x_j} + \frac{\partial u_j''}{\partial x_i} \right)} = 2\overline{p' s_{ij}''}, \tag{5}$$

is particularly strong. The production term and the pressure-strain rate of the streamwise Reynolds stress $\overline{\rho} R_{11}$ are shown in Figs. 12 and 13 normalized by ρ_0, Δu and the vorticity thickness δ_ω. Both, compressibility and heat release strongly attenuate production and redistribution of fluctuating kinetic energy. A similar reduction can be observed for the pressure-strain rates of the other diagonal Reynolds stresses as well.

(p, T, ρ)-fluctuations

The described attenuation of pressure-strain correlations by compressibility and heat release can be traced back to

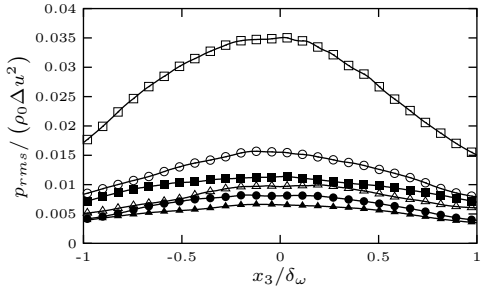

Figure 14: Rms value of pressure fluctuations, normalized by $\rho_0 \Delta u^2$, symbols as in Fig. 7

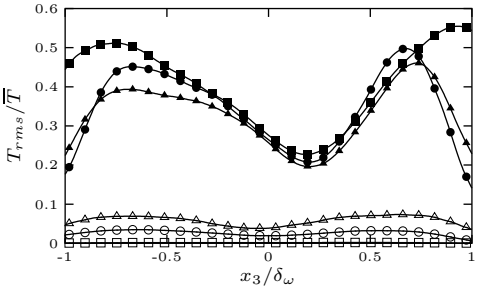

Figure 15: Rms value of temperature fluctuations, normalized by $\overline{T}$, symbols as in Fig. 7

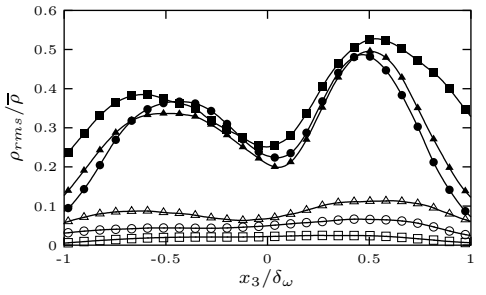

Figure 16: Rms value of density fluctuations, normalized by $\overline{\rho}$, symbols as in Fig. 7

the attenuation of pressure fluctuations which is stronger than the reduction of fluctuating velocity gradients and the changes in their correlation coefficients. The rms pressure fluctuations are displayed in Fig. 14.

The behaviour of the temperature and density fluctuations can be seen in Figs. 15 and 16. Heat release clearly enhances density and temperature fluctuations and strengthens their coupling which manifests itself in similar profiles of their rms values.

Reduction of pressure-strain correlations

In order to explain the reduction of the pressure-strain correlations Π_{ij}, an equation determining p' is derived. It is obtained by taking the divergence of the momentum equation, introducing the continuity equation and subtracting the averaged resulting equation. This leads to:

$$\frac{\partial^2 p'}{\partial x_j^2} = \underbrace{-\overline{\rho} \frac{\partial^2}{\partial x_i \partial x_j} \left(u_i'' u_j'' - \overline{u_i'' u_j''} \right)}_{A_1} \underbrace{-2\overline{\rho} \frac{\partial \widetilde{u}_1}{\partial x_3} \frac{\partial u_3''}{\partial x_1}}_{A_2} + A_3 + A_4 + B_1 + B_2 + B_3 + C_1 + \ldots + C_5 + \underbrace{\frac{D^2 \rho'}{Dt^2}}_{C_6} + \underbrace{\frac{\partial^2 \tau_{ij}'}{\partial x_i \partial x_j}}_{D} \tag{6}$$

The terms on the right hand side (RHS) can be grouped into four categories: The A-terms depend on the mean density. It will be shown in the following that the most important ones are A_1 and A_2. The other terms on the RHS, i.e. the B-, C- and D-terms are only present in compressible or reacting flows and involve density and viscous stress fluctuations. Term D, which is the second derivative of the fluctuating stress tensor, τ_{ij}', turns out to be very small for the cases studied in this work and can therefore be neglected. Term

C_6 contains pressure fluctuations as well as an explicit contribution of the heat release term for reacting flows:

$$\frac{D^2\rho'}{Dt^2} = \frac{1}{\overline{c}^2}\frac{D^2p'}{Dt^2} - \frac{1}{\overline{c_pT}}\frac{DQ'}{Dt} + h.o.t. \tag{7}$$

c denotes the sonic speed and c_p the heat capacity of the gas mixture at constant pressure. Q' denotes fluctuations of the heat release term Q,

$$Q = -\sum_{\alpha} \rho h_\alpha \frac{DY_\alpha}{Dt} \tag{8}$$

with h_α being the enthalpy of species α and DY_α/Dt the substantial derivative of its mass fraction Y_α. Provided the first term on the RHS of Eq. (7) plays a role, it makes Eq. (6) a convective wave equation. Such an equation was studied for non-reacting mixing layers by Pantano and Sarkar (2002). In our simulations, the correlation coefficient of ρ' and T' is negative for all Mach numbers under investigation. This indicates that acoustic effects are small, and hence the first term on the RHS of Eq. (7) is negligible. Equation (6) then becomes a Poisson equation,

$$\frac{\partial^2 p'}{\partial x_j^2} = f, \tag{9}$$

with all terms on the RHS of Eq. (6) being summarized in the source term f. After performing a Fourier transformation in the homogeneous directions, $p(x_1, x_2, x_3) \rightarrow \hat{p}(k_1, k_2, x_3)$, and a coordinate transformation in the direction of the main shear, $\breve{x}_3 = 2x_3/L_3$, Eq. (9) becomes

$$\left(\frac{d^2}{d\breve{x}_3^2} - k_1^2 - k_2^2\right)\hat{p}(k_1, k_2, \breve{x}_3) = \hat{f}(k_1, k_2, \breve{x}_3) \quad \text{with} \quad \left.\frac{\partial \hat{p}}{\partial \breve{x}_3}\right|_{\breve{x}_3=\pm 1} = 0. \tag{10}$$

This equation can be solved with a Green function G (Kim, 1989),

$$p'(x_1, x_2, \breve{x}_3) = \int_{-1}^{1} G * f\left(x_1, x_2, \breve{\breve{x}}_3\right) d\breve{\breve{x}}_3 \tag{11}$$

where the convolution $G * f$ represents the inverse Fourier transform of $\hat{G}\hat{f}$. Multiplication with $2s''_{ij}$ and statistical averaging results in the pressure-strain correlations

$$\Pi_{ij}(\breve{x}_3) = 2\int_{-1}^{1} \overline{G * f\left(x_1, x_2, \breve{\breve{x}}_3\right) s''_{ij}(x_1, x_2, \breve{x}_3)} d\breve{\breve{x}}_3 \tag{12}$$

When inserting not the complete RHS f into Eq. (9), but only a part of it, e.g. term A_1, it is possible to see which of the terms contribute most to the pressure fluctuations and to what mechanisms the reduction of the pressure-strain correlations is due. Figure 17 shows the contributions to the pressure-strain term Π_{11} for case inert-0.15. Obviously only terms A_1 and A_2 are significant and all other terms can be neglected. When summing up all contributions, the result, shown as a solid line in Fig. 18, corresponds well to the directly evaluated Π_{11} (dashed line). When increasing M_c (cf. Fig. 19), the contribution from term C_2, which is one of the terms involving density fluctuations, starts to grow. However, it remains small compared to the contributions from

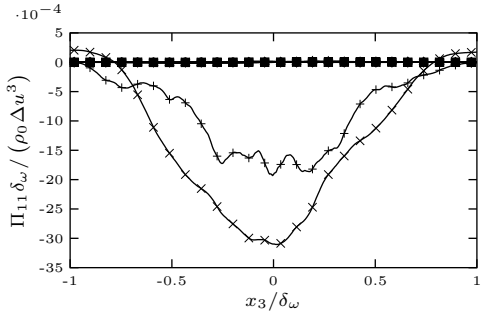

Figure 17: Case inert-0.15: Parts of the pressure-strain correlation Π_{11} computed with the Green function. +: $f = f(A_1)$, ×: $f = f(A_2)$, ∗: $f = f(A_3)$, □: $f = f(A_4)$, ■: $f = f(B_1)$, ○: $f = f(B_2)$, ●: $f = f(B_3)$, △: $f = f(C_1)$, ▲: $f = f(C_2)$, ▽: $f = f(C_3)$, ▼: $f = f(C_4)$, ⋄: $f = f(C_5)$

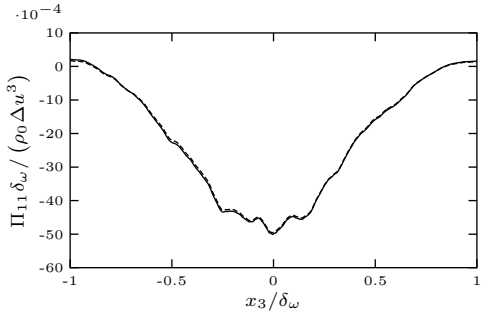

Figure 18: Case inert-0.15: Pressure-strain correlation Π_{11}. Solid: computed with the help of the Green function with $f = f\left(\sum_{i=1}^{4} A_i + \sum_{i=1}^{3} B_i + \sum_{i=1}^{5} C_i\right)$, dashed: evaluated directly

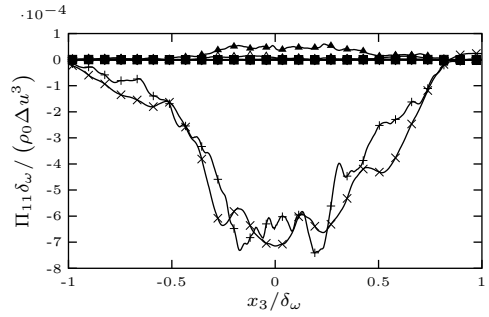

Figure 19: Case inert-1.1: Parts of the pressure-strain correlation Π_{11} computed with the Green function. Symbols as in Fig. 17

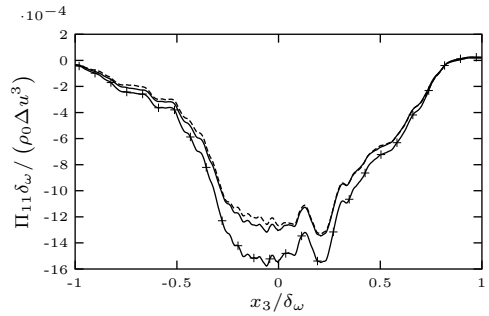

Figure 20: Case inert-1.1: Pressure-strain correlation Π_{11}. Solid, no symbols: computed with the help of the Green function with $f = f\left(\sum_{i=1}^{4} A_i + \sum_{i=1}^{3} B_i + \sum_{i=1}^{5} C_i\right)$, dashed, no symbols: evaluated directly, solid with symbols: computed with the help of the Green function with $f = (A_1 + A_2)$ and constant density

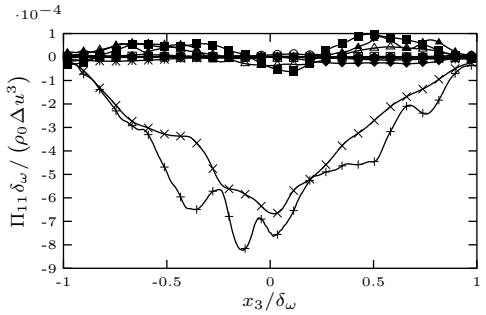

Figure 21: Case inf-0.15: Parts of the pressure-strain correlation Π_{11} computed with the Green function. +: $f = f(A_1)$, ×: $f = f(A_2)$, ∗: $f = f(A_3)$, □: $f = f(A_4)$, ■: $f = f(B_1)$, ○: $f = f(B_2)$, ●: $f = f(B_3)$, △: $f = f(C_1)$, ▲: $f = f(C_2)$, ▽: $f = f(C_3)$, ▼: $f = f(C_4)$, ◇: $f = f(C_5)$, ◆: $f = f(C_6)$

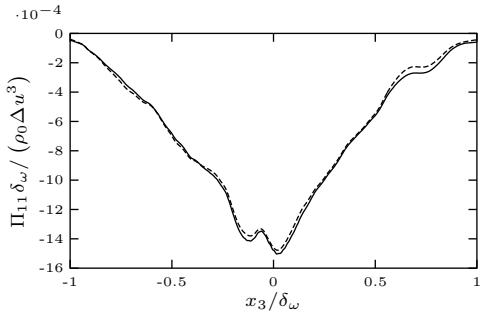

Figure 22: Case inf-0.15: Pressure-strain correlation Π_{11}. Solid: computed with the help of the Green function with $f = f\left(\sum_{i=1}^{4} A_i + \sum_{i=1}^{3} B_i + \sum_{i=1}^{6} C_i\right)$, dashed: evaluated directly

terms A_1 and A_2. Even though fluctuating pressure effects in term C_6 are neglected, the summation of the remaining terms provides still a good approximation to Π_{11} as shown in Fig. 20 since term C_6 is one order of magnitude smaller than A_1. Similar results are obtained for the remaining Π_{ij}-terms.

Figure 21 shows the contributions to the pressure-strain term Π_{11} for case inf-0.15. As for the inert mixing layer (cf. Fig. 17), the contributions from terms A_1 and A_2, which depend on the mean density, are the largest ones. The other contributions, even though non-zero, are small compared to A_1 and A_2. This is also the case for term C_6, which contains the heat release term explicitly. Again, despite neglecting fluctuating pressure effects, the summation of all terms that are shown in Fig. 21 provides a good approximation to Π_{11} (cf. Fig. 22).

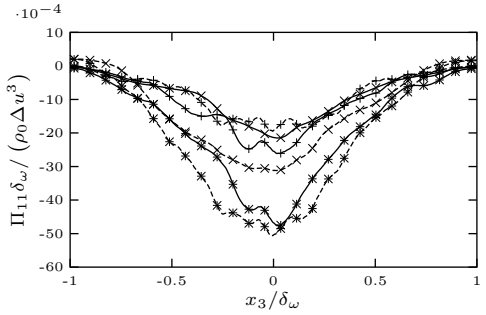

Figure 23: Parts of the pressure-strain correlation Π_{11} computed with the Green function and constant density ρ_0. Solid lines: case inf-0.15, dashed lines: case inert-0.15, +: $f = f(A_1)$, ×: $f = f(A_2)$, ∗: $f = f(A_1 + A_2)$

The complete pressure-strain rate Π_{11}, as well as the contributions from terms A_1 and A_2, are reduced significantly by heat release (compare Figs. 17 and 18 to Figs. 21 and 22). To find out, whether this is a consequence of the reduced mean density (cf. Fig. 8), which appears as a factor in terms A_1 and A_2, ρ_0 instead of $\overline{\rho}$ is inserted into the terms on the RHS of Eq. (6). Density fluctuations are set to zero. Figure 23 shows the contributions to Π_{11} when performing these modifications for the cases with $M_c = 0.15$: Now, the contributions from terms A_1 and A_2 have approximately the same size for the inert and reacting mixing layers. Since similar observations can be made for all pressure-strain correlations evaluated with constant ρ_0, it can be concluded that the reduction of Π_{ij} by heat release is predominantly a mean density effect. In contrast to this, the reduction of Π_{11} when M_c increases from 0.15 to 1.1 is only to a small extent a mean density effect, as seen in Fig. 20 where Π_{11} has been evaluated with constant ρ_0 for comparison. The dominant effect is due to changes in the fluctuating velocity field, e.g. the part $\left(u_i''u_j'' - \overline{u_i''u_j''}\right)$ of term A_1 (cf. Figs. 18 and 20).

SUMMARY AND CONCLUSIONS

DNS of inert and reacting compressible turbulent mixing layers at three different convective Mach numbers (M_c = 0.15, 0.7 and 1.1) have been performed and analyzed. It has been found that the effects of compressibility and heat release on the turbulence structure have the same tendencies, but different reasons: Both lead to a smoothening of the instantaneous flow fields, a reduction of the momentum thickness growth rate and of the turbulence fluctuations. However, there are qualitative differences between both effects: The reduction of the turbulent kinetic energy by heat release is due to the strong decrease of mean density around the flame sheet and therefore a mean density effect. The same can be said about the production rates and the pressure-strain correlations in the Reynolds stress transport equations. In contrast to this, the stabilizing effect of compressibility is mostly due to changes in the fluctuating velocity field.

REFERENCES

Foysi, H., Sarkar, S., and Friedrich, R., 2004, "Compressibility effects and turbulence scaling in supersonic channel flow", *J. Fluid Mech.* Vol. 509, pp. 207-216.

Kim, J., 1989, "On the structure of pressure fluctuations in simulated turbulent channel flow", *J. Fluid Mech.* Vol. 205, 421-451.

Pantano, C., and Sarkar, S., 2002, "A subgrid model for nonlinear functions of a scalar", *J. Fluid Mech.* Vol. 451, pp. 329-371.

Sarkar, S., 1995, "The stabilizing effect of compressibility in turbulent shear flow", *J. Fluid Mech.* Vol. 282, pp. 163-186.

Vreman, A.W., Sandham, N.D., and Luo, K.H., 1996, "Compressible mixing layer growth rate and turbulence characteristics", *J. Fluid Mech.* Vol. 320, pp. 235-258.